A tetranuclear nickel hydride cluster capable of reversible activation of aromatic and aliphatic C–H bonds

nature communications

Article

https://doi.org/10.1038/s41467-026-76006-4

A tetranuclear nickel hydride cluster capable of reversible activation of aromatic and aliphatic C–H bonds

Received: 21 October 2025

Accepted: 14 July 2026

Published online: 29 July 2026

Check for updates

Kohei Sunami[1], Tatsuya Higaki[1,6] ✉, Kanata Tanaka[1], Ryotaro Yamanashi[1], W. M. C. Sameera[2] ✉, Ryo Takahata[1], Toshiharu Teranishi[1], Soichi Kikkawa[3], Seiji Yamazoe[3], Takuya Shiga[4], Masayuki Nihei[4], Tatsuhisa Kato[5], Hitoshi Izu[1] & Yasuhiro Ohki[1] ✉

Metal cluster complexes supported by multiple hydrides are useful for activating inert bonds and molecules, while nickel-based variants capable of activating external substrates remain scarce. Here, we report a tetranuclear Ni-hydride-phosphine cluster, $[Ni_4H_4(P^tBu_3)_4]$ (**1**), which we synthesize by reacting $[Li(THF)_x][Ni\{N(SiMe_3)_2\}_3]$ ($x \approx 4.5-5$) with pinacolborane (HBpin) in the presence of tri-*tert*-butylphosphine (P^tBu_3). Its molecular structure features a tetrahedral Ni_4 core, with four face-capping μ_3-hydrides and four terminally bound P^tBu_3 ligands. Cluster **1** is capable of reversible C–H and C–D bond cleavage of benzene-d_6, toluene-d_8, *n*-octane-d_{18}, and its own P^tBu_3 ligands at 50 °C, leading to H/D exchange between the deuterated solvents and the ligands in **1**. This reactivity is further utilized in the catalytic hydrogen isotope exchange reaction between benzene-d_6 and toluene. The reversible dissociation of one P^tBu_3 ligand in **1** is proposed as the key step to trigger the C–H and C–D bond activation. Quantum chemical computations propose the reversible displacement of one of the P^tBu_3 ligands in **1** as the key step in triggering C–H and C–D bond activation.

Metal hydride clusters have attracted significant attention due to their unique reactivity, which arises from the cooperation between metal centers and hydrides[1–16]. For instance, $[(Cp^LTi)_3(\mu\text{-}H)_6(\mu_3\text{-}H)]$ (**[Ti$_3$]**; $Cp^L = C_5Me_4SiMe_3$) has been shown to react with N_2 via reductive H_2 elimination and N ≡ N triple bond cleavage[17,18], forming nitride species that undergo hydroamination in the presence of alkenes[19]. Our group has demonstrated that $[Fe_6(\mu\text{-}H)_{10}(\mu_3\text{-}H)_2(PMe_3)_6]$ (**[Fe$_6$]**) can catalytically convert N_2 to $N(SiMe_3)_3$ with a high turnover number (TON) of 183 ± 18 equiv. per cluster[20]. These examples highlight the potential of metal hydride clusters as platforms for activating and transforming inert molecules. Among transition-metal hydride clusters, nickel-based species are of interest due to their unique reactivity toward hydrocarbons[21,22]. For example, Johnson et al. reported $[Ni_5H_6(P^iPr_3)_5]$ (**[Ni$_5$]**), which can cleave C = C bonds of alkenes such as ethylene and styrene at temperatures as low as −30 °C[23]. These reactions proceed with near-quantitative yields and high selectivity, even in the presence of other reactive functional groups such as alcohols and amines. Moreover, **[Ni$_5$]** has been found to activate aromatic C–H bonds under mild conditions[24,25]. Despite these advances, nickel hydride clusters capable of activating external substrates remain scarce, partly because of the relatively weak Ni–C bonds compared to those of heavier metals[26] and the limited structural diversity of nickel hydride clusters.

[1]Institute for Chemical Research, Kyoto University, Gokasho, Uji, Japan. [2]Department of Physics and Astronomy, Chalmers University of Technology, Gothenburg, Sweden. [3]Department of Chemistry, Graduate School of Science, Tokyo Metropolitan University, Hachioji, Japan. [4]Department of Chemistry, Institute of Pure and Applied Sciences, University of Tsukuba, Ibaraki, Japan. [5]Fukui Institute for Fundamental Chemistry, Kyoto University, Kyoto, Japan. [6]Present address: Department of Chemistry, Graduate School of Science, Tokyo Metropolitan University, Hachioji, Japan. ✉e-mail: higaki-tatsuya@tmu.ac.jp; chamil@chalmers.se; ohki@scl.kyoto-u.ac.jp

Nevertheless, in a broader context, nickel-containing clusters have been explored for various applications, including alkyne semihydrogenation[12], H_2 activation[27,28], cyclization reactions[29,30], catalytic N_2 reduction[31,32], and the synthesis of electro-conductive nanosheets[33], demonstrating the potential of nickel as a versatile functional element in cluster chemistry.

Herein, we report a phosphine-protected nickel-hydride cluster, $[Ni_4H_4(P^tBu_3)_4]$ (**1**), featuring a tetrahedral Ni_4 core coordinated by four terminal P^tBu_3 ligands and four face-capping hydrides. Interestingly, cluster **1** mediates H/D exchange between its hydride/phosphine ligands and deuterated solvents, such as C_6D_6 and *n*-octane-d_{18}, via reversible C–H(D) bond activation. Heating a solution of **1** in a mixture of benzene-d_6 and toluene resulted in the isotope exchange, with **1** serving as the catalyst. This work paves the way for further exploration of nickel-hydride clusters with structural diversity and unique reactivity.

Results

Synthesis and crystal structure of $Ni_4H_4(P^tBu_3)_4$ (1)

Typical synthetic methods for nickel-hydride clusters involve reactions of Ni complexes with H_2 or hydride reagents[34–41]. For example, Johnson et al. synthesized **[Ni$_5$]** by reacting an N_2-bridged Ni complex $[(^iPr_3P)_2Ni]_2(\mu\text{-}N_2)$ with H_2[24], and a tetranuclear hydride-chloride cluster $[(^iPr_3P)_2Ni]_4H_4Cl_2$ from a related reaction of $[(^iPr_3P)_2Ni]_2(\mu\text{-}N_2)$ with $(^iPr_3P)_2NiCl_2$ and H_2[34]. A cyclopentadienyl (Cp)-supported tetrahedral Ni hydride cluster, $[(CpNi)_4H_3]$ was synthesized by reacting CpNi(NO) with $AlCl_3$ and $LiAlH_4$[35,36]. Pasynkiewicz et al. reported the synthesis of $[(CpNi)_4H_2]$ by reacting nickelocene and phenyllithium in the presence of 1-decene[37]. As such, nickel-hydride clusters prepared by conventional methods are typically stabilized by ligands originating from the starting Ni complexes. Although exceptions exist, such as the work by Schneider et al. on the synthesis of $[(Cp^RNi)_4H_n]$ ($n = 1$ or 3; $Cp^R = C_5H_4{}^tBu$) by vaporizing nickel atoms into solutions of substituted Cp ligands[38], these methods are less practical due to the harsh conditions required to generate atomic Ni.

Recently, our group developed a facile method for the synthesis of metal hydride clusters by treating metal(II) bis-amide complexes $M\{N(SiMe_3)_2\}_2$ with pinacolborane (HBpin) in the presence of phosphines. For example, **[Fe$_6$]** was synthesized via the reaction of $Fe\{N(SiMe_3)_2\}_2$ with HBpin and PMe_3[20]. This reaction proceeds through σ-bond metathesis, forming "Fe–H" intermediates for cluster growth and an inert byproduct $(Me_3Si)_2N\text{–}Bpin$[42]. This synthetic approach has also been successfully applied to the synthesis of a nanometer-sized iron-hydride cluster $[Fe_{55}H_{46}(P^tBu_3)_{12}]^{+}$[43], as well as cobalt-hydride clusters including $[Co_6H_8(P^iPr_3)_6]$[5]. Additionally, Jacobi von Wangelin et al. developed a related protocol, using diisobutylaluminum hydride instead of HBpin for iron-hydride cluster synthesis[9,44]. With these successful examples, we sought to extend this methodology to synthesize new nickel-hydride clusters. However, the instability of the nickel precursor $Ni\{N(SiMe_3)_2\}_2$, which decomposes gradually at room temperature[45], prevented its direct application. The tetrameric complex $[Ni\{N(SiMe_3)_2\}]_4$ has been reported[45], but we have been unable to synthesize it on a gram scale. We then tested an alternative two-coordinate complex reported by Don Tilley et al., $Ni\{N(SiMe_3)(DIPP)\}_2$ (DIPP = 2,6-diisopropylphenyl)[46], but this approach was unsuccessful due to the steric hindrance of the DIPP groups, which slowed the approach of HBpin to the nickel center, preventing the formation of "Ni–H" intermediates at a sufficient rate. Under these circumstances, a tris-amide complex, $[Li(THF)_x][Ni\{N(SiMe_3)_2\}_3]$ ($x \approx 4.5-5$) (**NiL$_3$**)[47], reported recently by Werncke et al., offered us a potential solution. This tris-amide complex **NiL$_3$** was found to reversibly dissociate one of its amide ligands in toluene, generating $Ni\{N(SiMe_3)_2\}_2$ and $LiN(SiMe_3)_2$. Inspired by this finding, we employed **NiL$_3$** for the in-situ generation of $Ni\{N(SiMe_3)_2\}_2$ and subsequent reactions with HBpin in the presence of phosphines.

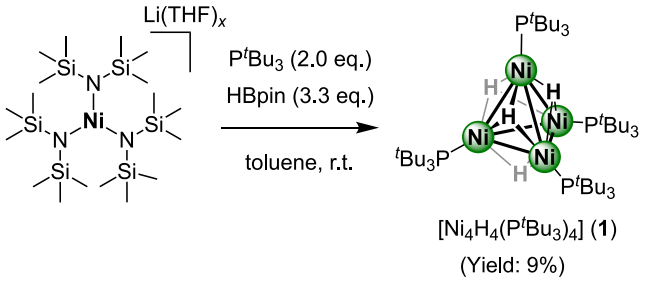

Fig. 1 | Synthesis of $[Ni_4H_4(P^tBu_3)_4]$ (1). Synthetic route to **1** from $[Li(THF)_x][Ni\{N(SiMe_3)_2\}_3]$ ($x = 4.5-5$), HBpin, and P^tBu_3. The relative stoichiometry of the reactants is indicated.

Treatment of a toluene solution of **NiL$_3$** with a slight excess of P^tBu_3 (2.0 equiv.) and HBpin (3.3 equiv.) at room temperature provided a black solution, from which a tetranuclear nickel-hydride cluster $[Ni_4H_4(P^tBu_3)_4]$ (**1**) was isolated (Fig. 1). Initially, crystals of **1·P^{t}Bu$_3$** containing an additional P^tBu_3 molecule incorporated in the crystal lattice were obtained as the primary crystalline product in 19% yield. Subsequent recrystallization from pentane yielded phosphine-free dark brown crystals of **1** in 9% yield. After separation of the first crop of **1·P^{t}Bu$_3$**, the supernatant was analyzed by mass spectrometry to reveal **1** (Supplementary Information Fig. S22), but attempts to obtain the second crop did not provide **1·P^{t}Bu$_3$** in a pure form. An analogous reaction was also attempted using P^iPr_3 to explore the potential alternative synthesis of **[Ni$_5$]**. However, **[Ni$_5$]** was not detected from this reaction mixture. The ^{1}H NMR spectrum of isolated **1** in C_6D_6 exhibited a broad signal of P^tBu_3 at 2.60 ppm (Supplementary Information Fig. S1), indicating the paramagnetic nature of **1** at ambient temperature. The hydride and phosphorus signals were not observed even at −80 °C, likely due to significant broadening induced by interactions with the magnetic (nickel) centers[5,9,20,43]. Nevertheless, the labile hydrogen atoms (hydrides) in **1** were quantified by thermolysis of crystalline **1** at 150 °C (Supplementary Information Tables S1–S2, Figs. S19–S21). The amount of released H_2 was measured as 2.24(8) equivalents per molecule of **1**, consistent with the presence of four hydrides.

Single crystals of **1·P^{t}Bu$_3$** were characterized by X-ray crystallographic analysis (Fig. 2A and Supplementary Information Table S3), and the molecular structure of phosphine-free **1** was similarly confirmed by X-ray analysis. In the crystal of **1·P^{t}Bu$_3$**, free P^tBu_3 was identified in addition to **1**. The Ni–Ni bond distances in **1** range from 2.3857(3) to 2.4549(3) Å, which are shorter than the typical Ni–Ni covalent bond length (*i.e.*, 2.48 Å)[48]. The formal oxidation state of metals in **1** is Ni(I), based on the chemical formula of $[Ni_4H_4(P^tBu_3)_4]$. The observed Ni–P bond distances in **1**, ranging from 2.1963(4) to 2.2128(4) Å, are consistent with those in formally Ni(I) phosphine complexes (Supplementary Information Table S4), further supporting the formal oxidation state of Ni(I) in **1**. The Ni_4 core is protected by face-capping μ_3-hydrides that are placed on each triangle facet of the tetrahedral Ni_4 structure. The positions of the hydrides were determined and refined from residual electron density during X-ray analysis. The presence of four hydrides was also confirmed by mass spectrometry (*vide infra*).

The Ni–Ni bond distances in **1** were compared with previously reported tetrahedral Ni_4 hydride clusters. For example, the Ni–Ni bond distances in $[(CpNi)_4H_3]$ range from 2.454(3)–2.490(3) Å, which are slightly longer than those in **1**. $[(CpNi)_4H_3]$ was also characterized by neutron diffraction, which revealed the positions of hydrides[49]. The neutron diffraction data showed Ni–Ni bond distances ranging from 2.478(3)–2.490(3) Å, consistent with those determined by X-ray crystallography. The Ni-H bond distances determined by neutron diffraction range from 1.661(9) to 1.720(8) Å.

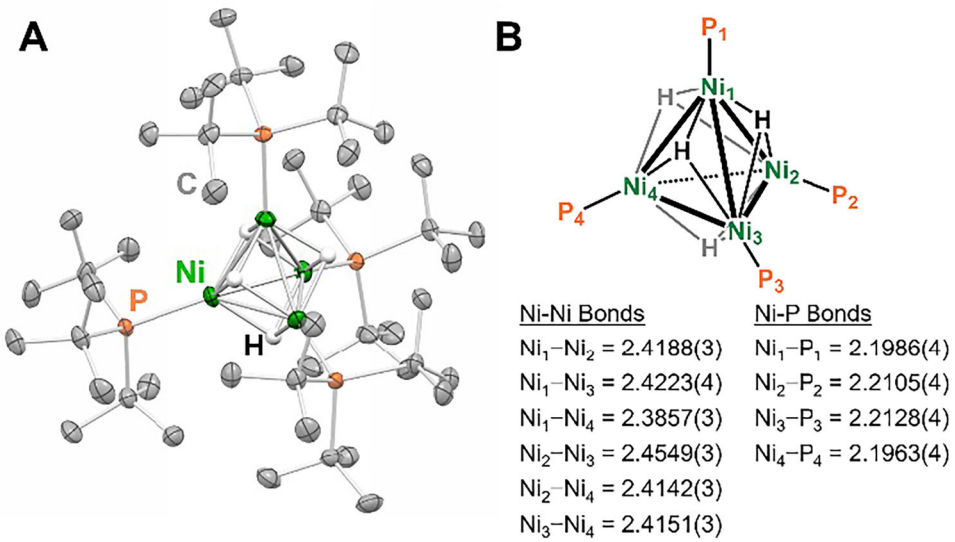

Fig. 2 | Crystal structure of 1·P^{t}Bu$_3$. A Crystal structure of **1**·P^{t}Bu$_3$ with atomic displacement parameters set at 50% probability. The co-crystallized P^{t}Bu$_3$ molecule and hydrogen atoms on the P^{t}Bu$_3$ ligands are omitted for clarity. **B** Selected bond distances (Å) and angles (°) in **1**: Ni–Ni 2.3857(3)–2.4549(3), Ni–P 2.1963(4)–2.2128(4); Ni–Ni–Ni 59.101(7)–61.105(9).

Magnetic properties and density functional theory calculations

The broad signal observed in the ^{1}H NMR spectrum of **1** suggests its paramagnetic nature at ambient temperature. To investigate its magnetic properties, the solution magnetism of **1** was analyzed using the Evans method[50,51]. The resulting magnetic moment of 1.8(3) μ_B at 298 K indicates partial population of the $S = 1$ state (expected spin-only moment: 2.83 μ_B) at ambient temperature. Further magnetic characterization of **1** was performed on solid-state samples using a superconducting quantum interference device (SQUID). Direct current (DC) magnetic susceptibility data collected on microcrystalline samples of **1** under a 1 T field revealed $\chi_M T$ values of 0.49 cm^{3}K/mol at 300 K and 0.0061 cm^{3}K/mol at 1.8 K, corresponding to μ_{eff} values of 2.0 and 0.22 μ_B, respectively. The μ_{eff} value at 300 K is consistent with the solution magnetic moment ($\mu_{eff} = 1.8(3)$ μ_B), while the value at 1.8 K indicates the $S = 0$ ground state (Supplementary Information Fig. S36). This $S = 0$ ground state assignment was further supported by the silent electron spin resonance (ESR) spectrum observed for microcrystalline samples at 4 and 8 K in the X-band mode (Supplementary Information Fig. S37).

Density functional theory (DFT) calculations on **1**, using the BP86-D3BJ functional[52,53], align with the experimentally determined ground state. Further, the $S = 0$, 1, and 2 spin states of **1** were optimized, revealing $S = 0$ as the ground state (Supplementary Information Table S6). Kohn-Sham frontier orbitals of the ground state are delocalized over nickel atoms (Supplementary Information Fig. S50), showing extensive orbital delocalization over the metal framework. Despite several attempts, we were unable to locate the broken symmetry singlet (or triplet) state, where the computations ultimately converged to the closed-shell singlet state. The $S = 1$ and 2 states were calculated to be 7.8 and 20.5 kcal mol^{-1} higher in energy than the ground state, respectively. The exact $S = 0/S = 1$ energy gap is sensitive to the computational method employed (*vide infra*); all calculations consistently predict the $S = 0$ state with low-lying excited spin states, in agreement with the observed magnetic properties of **1**. The calculated $\langle S^2 \rangle$ value for the $S = 1$ state is 2.01, which is in close agreement with the theoretical value of 2.00. This result confirms the absence of spin contamination. The computed spin densities on the nickel centers in the $S = 1$ state are ρ(Ni1) = 0.43, ρ(Ni2) = 0.44, ρ(Ni3) = 0.42, and ρ(Ni4) = 0.26, indicating that the unpaired electrons are primarily delocalized across the four nickel atoms.

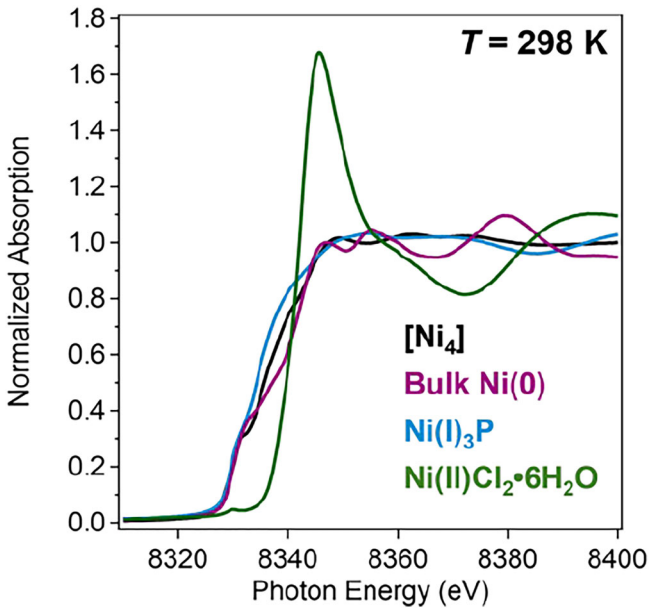

Fig. 3 | Ni *K*-edge XANES spectra of 1 and reference compounds. Ni *K*-edge XANES spectra of Ni foil, Ni_3P, Ni(II)Cl_2·$6H_2O$ and **1** recorded at 298 K. **[Ni$_4$]** = [Ni_4H_4(P^{t}Bu$_3$)$_4$] (**1**).

X-ray absorption fine structure (XAFS) analysis

To further verify the electronic structure of Ni atoms in **1**, Ni *K*-edge X-ray absorption fine structure (XAFS) was measured at a synchrotron facility. Solid samples were sealed in plastic films, placed in aluminum bags, and their spectra were measured in transmission mode. For comparison, some standard samples such as Ni(0) foil, Ni(I)$_3$P, and Ni(II)Cl_2·$6H_2O$ were also measured. The onset of the X-ray absorption near edge structure (XANES) spectra, which corresponds to the electronic structure of Ni, shifts to higher energy from Ni(0) to Ni(II) (Fig. 3). The absorption onsets of Ni(0) foil and Ni(I)$_3$P are very similar, indicating that Ni atoms in Ni_3P have almost metallic electron density, as reported previously[54,55]. The similarity of the absorption onset between Ni_3P and **1** further suggests a relatively high electron density

https://doi.org/10.1038/s41467-026-76006-4

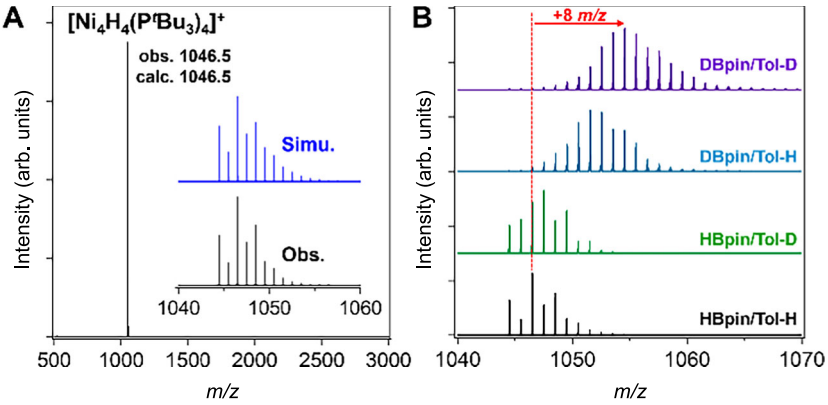

Fig. 4 | Positive-mode ESI-MS characterization of 1 and its deuterated analogue. A Positive-mode ESI-MS spectrum of **1**. The inset shows the simulated isotope pattern. **B** Positive-mode ESI-MS spectrum of deuterated **1** synthesized using DBpin and/or toluene-d_8. Tol-H = toluene and Tol-D = toluene-d_8.

in the Ni atoms of **1**. The two XANES spectra of **1** recorded at 298 and 123 K are nearly identical, probably due to the negligible temperature dependence of the electronic structures within the observed temperature range (Supplementary Information Fig. S38).

Extended X-ray absorption fine structure (EXAFS) analysis of the standard samples was compared with that of **1** to investigate the local environment of the nickel centers (Supplementary Information Fig. S39). The EXAFS spectra of Ni(0) foil and $Ni(I)_3P$, which feature the Ni–Ni or Ni–P bonds, exhibited oscillations with similar periodicity. This similarity complicated the curve-fitting analysis of **1**, which contains both Ni–Ni and Ni–P bonds (Supplementary Information Fig. S40). Nevertheless, the FT-EXAFS data of **1** at 298 K yielded the r values (bond lengths) of 2.37(4) Å for Ni–Ni and 2.20(5) Å for Ni–P bonds (Supplementary Information Table S5), in agreement with overlapping peaks in the FT-EXAFS spectrum. These r values remained constant at 123 K, with values of 2.37(3) and 2.19(4) Å for Ni–Ni and Ni–P bonds. These r values are consistent with the crystallographic Ni-Ni and Ni-P bond distances (Ni–Ni: 2.3857(3)−2.4549(3) Å, Ni–P: 2.1963(4)−2.2128(4) Å).

ESI-MS analysis of 1 and deuterated 1

The molecular formula of **1**, including four hydrides, was further confirmed by ESI-MS analysis. The positive-mode spectrum exhibited a signal at $m/z = 1046.5$, with an isotope pattern closely matching the simulated pattern for $[Ni_4H_4(P^tBu_3)_4]^+$ ($[\mathbf{1}]^+$, $m/z = 1046.5$) (Fig. 4A). To investigate deuterium incorporation and its origin, ESI-MS analysis was also performed for deuterated samples of **1**. The deuterated sample synthesized using DBpin[56] in toluene-d_8 gave a signal at $m/z = 1058.6$ (Fig. 4B, purple, and Supplementary Information Fig. S24), indicating a shift of +8 units compared to **1**. This shift suggests an average of 8 H/D exchanges during synthesis. As this shift exceeds the number of hydrides in **1**, it indicates deuterium incorporation into both hydrides and the P^tBu_3 ligands. The isotope pattern of deuterated **1** was broader due to variations in the number of incorporated deuterium atoms. Additional experiments were performed using DBpin in non-deuterated toluene and yielded a signal at $m/z = 1051.5$ (Fig. 4B, blue), corresponding to an average of 5 H/D exchanges. This result indicates that deuterium atoms were derived from both pinacolborane and toluene. Thus, when HBpin was used in toluene-d_8, the ESI-MS spectrum showed an average m/z shift of +1 unit (Fig. 4B, green), confirming that deuterium incorporation in this case was primarily from toluene through C–D bond activation.

Reversible C–H(D) bond activation of aromatic and aliphatic hydrocarbons mediated by 1

The ESI-MS analysis of deuterated **1** (Fig. 4) revealed evidence of C–H(D) bond activation of the P^tBu_3 ligands and toluene-d_8. This finding prompted us to investigate the C–H(D) bond activation of non-functionalized aromatic and aliphatic hydrocarbons, such as C_6D_6 and *n*-octane-d_{18}, through hydrogen isotope exchange reactions.

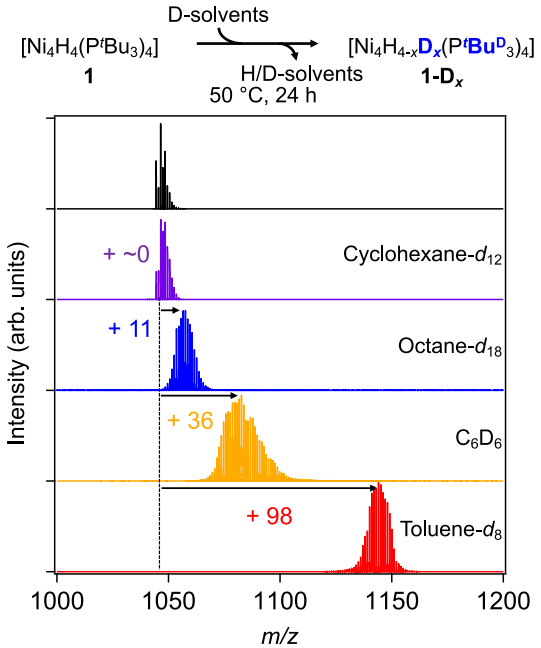

Fig. 5 | Deuterium incorporation into 1 upon reaction with deuterated hydrocarbons. ESI-MS spectra showing deuterium incorporation into **1** through H/D exchange with cyclohexane-d_{12}, *n*-octane-d_{18}, C_6D_6, and toluene-d_8 after heating at 50 °C for 24 h. $^tBu^D$ = partially deuterated ^tBu.

Heating a C_6D_6 solution of **1** at 50 °C for 24 h resulted in a shift of the ESI-MS signals by +36 units, exhibiting a broad signal with the highest peak at $m/z = 1082.7$ (Fig. 5, orange and Supplementary Information Fig. S25). The shift of +36 units corresponds to 36 H/D exchanges between the hydrides and P^tBu_3 ligands in **1** and C_6D_6. Deuterium incorporation into the P^tBu_3 ligands was further verified by ^2H NMR analysis of deuterated **1** prepared from the reaction with C_6D_6 (Supplementary Information Fig. S8). The H/D exchange was facilitated in toluene-d_8, leading to 98 H/D exchanges under identical conditions at 50 °C for 24 h (Fig. 5, red). Extending the reaction time to 72 h led to nearly complete deuteration, producing $[Ni_4D_4(PC_{12}D_{-27})_4]$ (**1-d_{-112}**) (Supplementary Information Fig. S26C). To further investigate the reaction behavior of **1** and evaluate the possible involvement of Ni

nanoparticles in the H/D exchange process, several control experiments were performed in C_6D_6. Although a mercury poisoning test was initially attempted, direct reaction between Hg and **1** prevented meaningful interpretation of the experiment. A hot filtration experiment showed that the H/D exchange proceeded at a comparable rate after removal of any insoluble material, suggesting that the observed reactivity does not require insoluble heterogeneous species (Supplementary Information Fig. S45). In addition, time-course analysis revealed no observable induction period and a steady increase in H/D exchange over 48 h (Supplementary Information Figs. S29 and S30). Furthermore, the H/D exchange became slower at higher concentrations of **1** and was significantly suppressed in the presence of externally added P^tBu_3 (Supplementary Information Fig. S28). These observations collectively support a homogeneous molecular pathway involving reversible phosphine displacement in **1** under the reaction conditions and argue against nanoparticle-mediated reactivity as the dominant H/D exchange pathway.

As aliphatic C–H bond activation of P^tBu_3 occurs reversibly during H/D exchange, we extended this study to investigate the C–H(D) bond activation of external alkanes, which represent a challenging class of substrates due to the absence of metal-coordinating groups. Commercially available *n*-octane-d_{18} was used as the deuterated solvent instead of C_6D_6, and the solution of **1** was heated under similar conditions at 50 °C (Fig. 5, blue). Although the reaction proceeded more slowly than with C_6D_6, 11 H/D exchanges were observed after 24 h between **1** and *n*-octane-d_{18}. In contrast, a similar reaction with cyclohexane-d_{12} at 50 °C for 24 h resulted in negligible exchange (Fig. 5, purple), indicating a preference for methyl C–H(D) bond activation. Although the origin of this substrate dependence remains unclear, the different reactivity of *n*-octane-d_{18} and cyclohexane-d_{12} may reflect the greater accessibility of primary C–H(D) bonds compared with the secondary C–H(D) bonds of cyclohexane. The ability of **1** to activate alkane C–H(D) bonds under relatively mild conditions at 50 °C is noteworthy, as representative rhodium and iridium complexes typically require temperatures of 100 °C or higher[57–63]. It is also notable that heterolytic C–H activation has proven effective with *aliphatic* C–H bonds at around 80 °C using a half-sandwich iridium complex[64]. Despite recent advances in C–H bond activation by nickel complexes[22,65,66], in addition to the *aromatic* C–H activation at 45 °C catalyzed by a (diamine)Ni complex[67], this study represents a rare example of thermally driven *aliphatic* C–H(D) bond activation of *n*-octane (and *tert*-butyl groups of the ligand) by a nickel complex under mild conditions. In contrast to mono-nuclear nickel complexes, multimetallic redox behavior of the four nickel centers in **1** can cooperatively accommodate the 2e-oxidation required for C–H oxidative addition, thereby facilitating C–H(D) activation.

The reversible activation of both aromatic and aliphatic C–H(D) bonds by **1** prompted us to explore its catalytic potential for H/D exchange between C_6D_6 and toluene. A toluene solution of **1** (0.2 mol%) was mixed with C_6D_6 (toluene/C_6D_6 = 1/5 by weight) and heated at 50 °C for 24 h (Fig. 6). The resultant ^1H and ^2H NMR spectra revealed deuterium incorporation into the methyl group of toluene (Supplementary Information Fig. S41), achieving a TON of 96 based on the intensity change in the methyl signal of toluene (19% methyl deuteration). When the reaction temperature was increased to 60 °C under otherwise identical conditions, the H/D exchange reaction was significantly accelerated, and the TON reached 211 after 24 h (42% methyl deuteration, Supplementary Information Fig. S44). Notably, the ^1H NMR signal of **1** was still observed after completion of the reaction, indicating that the cluster remains intact under these conditions. GC-MS analysis of the reaction mixture revealed an increase in the *m/z* of toluene, further confirming the deuterium incorporation (Supplementary Information Fig. S43). A similar catalytic reaction was attempted using *n*-octane-d_{18} instead of C_6D_6, but no evidence of deuteration was observed under the same conditions, indicating that

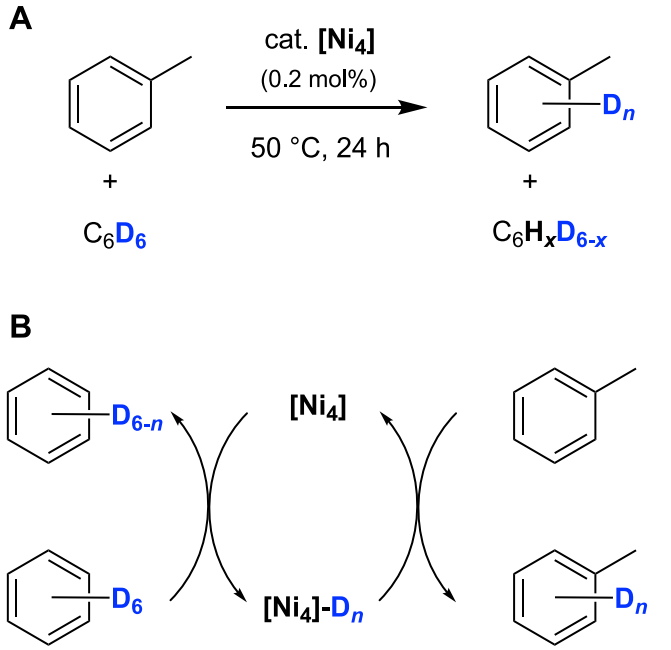

Fig. 6 | Catalytic H/D exchange mediated by 1. A Catalytic H/D exchange between toluene and C_6D_6 mediated by **1**. **B** Proposed reaction pathway involving initial H/D exchange between **1** and C_6D_6, followed by subsequent H/D exchange between the resulting deuterated **1** and toluene. [Ni_4] = [$Ni_4H_4(P^tBu_3)_4$].

the C–H activation of *n*-octane by **1** is significantly slower than that of toluene. At higher temperatures (e.g. 100 °C), **1** gradually decomposed to form insoluble materials, preventing confirmation of its catalytic activity. Further attempts to functionalize hydrocarbons catalytically, such as the C–H borylation[56], ended up with the decomposition of the nickel cluster and gave insoluble materials.

Mechanistic insights and computed reaction pathways

The ^1H NMR spectrum of **1** (Supplementary Information Fig. S1) consistently exhibited a minor signal of free P^tBu_3, even in isolated phosphine-free crystalline samples. This observation is consistent with phosphine displacement during substrate coordination. To examine the possibility of reversible ligand dissociation, a ligand exchange experiment was performed using PCy_3 (Cy = cyclohexyl), which possesses electronic and steric properties similar to those of P^tBu_3. In the presence of 3 equiv. of PCy_3, a benzene solution of **1** was heated at 50 °C. After 1 h, the ESI-MS spectrum of the reaction mixture revealed an intense signal corresponding to the ligand-exchange product, $[Ni_4H_4(P^tBu_3)_3(PCy_3)]^+$ (*m/z* = 1124.5), in addition to unreacted **1** (Fig. 7). This result confirms that one of the P^tBu_3 ligands of **1** exchanges with external ligands or substrates at 50 °C in solution.

The H/D exchanges between hydrides in **1** and toluene-d_8 or C_6D_6 occurred even at room temperature, as was indicated by the appearance of multiple signals of methyl and quaternary carbons in the ^{13}C NMR (Supplementary Information Figs. S5 and S6), while this phenomenon was not observed in the ^{13}C NMR measured in C_6H_6 (Supplementary Information Fig. S4). Heating of the solution of **1** in toluene-d_8 at 50 °C resulted in the appearance of more complicated signals (Supplementary Information Fig. S6), indicating the deuterium incorporation into the ^{t}Bu groups. These results indicate that the C–H activation barrier for the ^{t}Bu groups is higher than those for toluene and benzene.

The discussion above indicates that the rate-determining step of the reaction is not the P^tBu_3 ligand dissociation from **1** but is more likely associated with the cleavage of C–H(D) bonds. To support this

hypothesis, we roughly estimated the kinetic isotope effect (KIE) for the overall reaction. This estimation was based on comparing the H/D exchange observed in the ESI-MS spectra for the reactions of **1** with C_6D_6 and $[Ni_4D_4(PC_{12}D_{-27})_4]$ (**1-*d*$_{-112}$**) with C_6H_6, as the paramagnetic nature of **1** at ambient temperature prevents accurate analysis of the H/D exchange kinetics by NMR. Heating a C_6H_6 solution of **1-*d*$_{-112}$** at 50 °C for 24 h resulted in the −20 *m/z* shift in the ESI-MS signal (Supplementary Information Fig. S26, pink), while the reaction of **1** with C_6D_6 under the same conditions led to the +36 *m/z* shift (Fig. 5, orange). Based on these results, the preliminary KIE for this reaction can be approximately estimated as 36/20 ≈ 1.8. Although this observation is consistent with the involvement of C–H(D) bond activation in the overall reaction process, the present data do not allow unambiguous assignment of the rate-determining step.

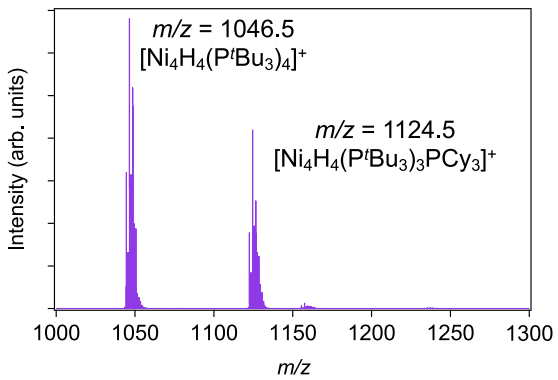

Fig. 7 | Ligand exchange between P^{t}Bu$_3$ in 1 and PCy$_3$. Positive-mode ESI-MS spectrum recorded after heating a benzene solution of **1** with PCy_3 (3 equiv.) at 50 °C for 1 h.

DFT calculations were performed to elucidate the mechanism of C–H bond activation of P^{t}Bu$_3$ and benzene (Figs. 8 and 9). The free energy profile for the intramolecular C–H bond activation (cyclometallation) of P^{t}Bu$_3$ is shown in Fig. 8, using the *S* = 0 state of **1** (^{1}**1**) as the reference point. The calculated *S* = 0 and *S* = 1 states for local minima and transition states in the profile are relatively close in energy. The spin-state energetics of **1** in Fig. 8 were obtained using ONIOM (BP86-D3BJ:GFN1-xTB), where the ^{t}Bu groups of three P^{t}Bu$_3$ ligands were treated in the ONIOM low-level to reduce computational cost. Energy gaps differ quantitatively from the full BP86-D3BJ calculations, although both methods predict the *S* = 0 state as the ground state. The *S* = 2 state was also calculated, but its contribution is negligible due to the significantly higher energy. The computed barrier for cyclometallation (^{1}**1** → ^{1}**TS1**) is 23.6 kcal mol^{-1}, and overcoming this barrier is possible by heating the reaction mixture at 50 °C. In agreement with this calculation, an overall activation energy of 26.8 kcal mol^{-1} was estimated by preliminary kinetic analysis of the H/D exchange reaction based on ESI-MS monitoring at 40–70 °C (Supplementary Information Figs. S31–32). The computed KIE for this process is 2.3, which is in qualitative agreement with the preliminary experimental value of 1.8. The transition state in the *S* = 1 state (^{3}**TS1**) lies only 0.5 kcal mol^{-1} above the *S* = 0 transition state (^{1}**TS1**). The resulting intermediate after cyclometallation (^{1}**I1**) lies 16.4 kcal mol^{-1} higher in energy than ^{1}**1**, suggesting that the reverse reaction to regenerate **1** is thermodynamically favored. These results support the feasibility of the proposed reaction pathway under the experimental conditions used in this study.

An initial step in substrate C–H activation likely involves displacement of a P^{t}Bu$_3$ ligand, as suggested by the ligand exchange reaction of **1** (Fig. 7). Consistent with this interpretation, the H/D exchange between **1** and C_6D_6 became progressively slower upon

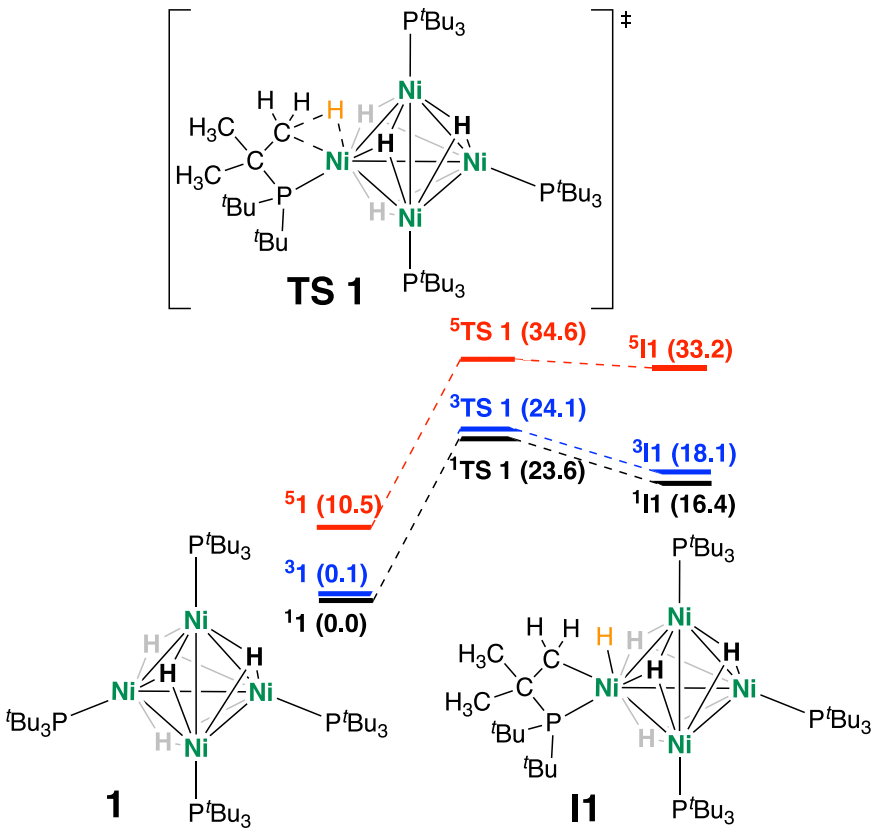

Fig. 8 | Free energy profile for the intramolecular C–H bond activation of P^{t}Bu$_3$. Relative free energies are given in kcal mol^{-1}. Superscripts denote the spin multiplicities. Calculations were performed using the ONIOM method with BP86-D3BJ/ZORA-def2-TZVP.

https://doi.org/10.1038/s41467-026-76006-4

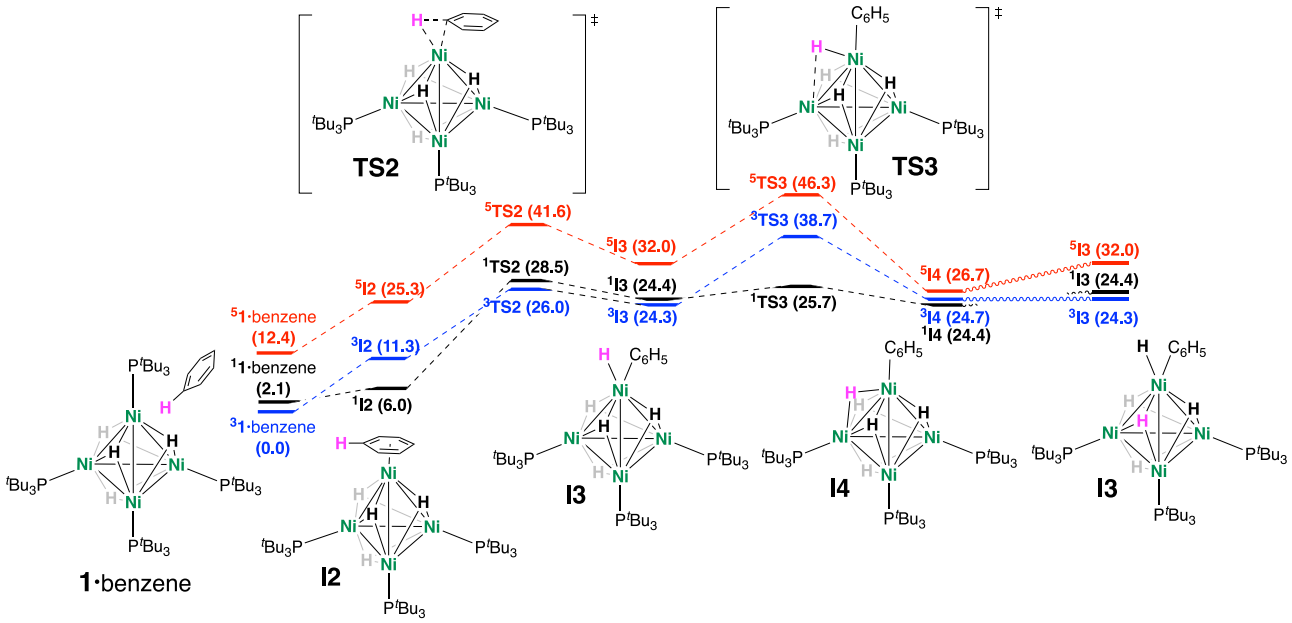

Fig. 9 | Free energy profile for C–H bond activation of benzene starting from 1·benzene. Relative free energies are given in kcal mol^{-1}. Superscripts denote the spin multiplicities. Calculations were performed using the ONIOM method with BP86-D3BJ/ZORA-def2-TZVP.

increasing the amount of externally added P^{t}Bu$_3$ from 1 to 10 equiv. under otherwise identical conditions (Supplementary Information Figs. S27C and S28). These observations are consistent with a mechanism in which substrate coordination is accompanied by displacement of a P^{t}Bu$_3$ ligand prior to subsequent C-H activation. The computed relaxed potential energy surface (Supplementary Information Fig. S52) indicates that the spontaneous dissociation of one P^{t}Bu$_3$ ligand from ^{1}**1** has a significantly higher barrier than an associative pathway in which Ni-P bond elongation and benzene binding occur simultaneously.

The computed free energy profile for the benzene C–H bond activation is summarized in Fig. 9. For these calculations, the reference state was chosen as **1·benzene** (^{3}**1·benzene** in the $S = 1$ state), which is the pre-associated reactant complex, rather than **1** alone. This choice allows for a meaningful comparison with the intramolecular C–H activation of P^{t}Bu$_3$ (Fig. 8), as it accounts for the significant entropy difference between intra- and inter-molecular processes.

Displacement of a P^{t}Bu$_3$ ligand upon substrate coordination, starting from ^{3}**1·benzene** and accompanied by a spin crossover from $S = 1$ to $S = 0$, affords the intermediate ^{1}**I2**, which lies 6.0 kcal mol^{-1} above the entry point. The corresponding $S = 1$ state ^{3}**I2** is 5.3 kcal mol^{-1} higher in energy than ^{1}**I2**. Subsequent C–H bond activation of benzene proceeds from ^{1}**I2**, also involving a spin crossover (^{1}**I2** → ^{3}**TS2**). The calculated free energy barrier for the C–H bond activation of benzene starting from ^{1}**I2** is 20.0 kcal mol^{-1}. Since this step corresponds to the H/D exchange process, we calculated the KIE and obtained a value of 1.8, which is in good agreement with the roughly estimated experimental value. The resultant intermediate ^{3}**I3** lies 18.3 kcal mol^{-1} above ^{1}**I2**. After C–H activation of benzene, migration of the terminal Ni–H hydride to a bridging position (^{3}**I3** → ^{1}**I4**) occurs with a low energy barrier of only 1.4 kcal mol^{-1}. The energy of ^{1}**I4** is comparable to that of ^{3}**I3**, suggesting that reversible migration between terminal and bridging hydrides is facile. Based on these computations, we conclude that the C–H activation of benzene from **1·benzene** proceeds via a pre-equilibrium involving ^{1}**I2**, while we have been unable to locate an optimized transition state. This pre-equilibrium is followed by a barrier of 20.0 kcal mol^{-1} (^{1}**I2** → ^{3}**TS2**), which is lower than that for the intramolecular cyclometallation of P^{t}Bu$_3$ (Fig. 8). The overall barrier of 26.0 kcal mol^{-1} (^{3}**1·benzene** → ^{3}**TS2**) is slightly higher than that for the cyclometallation. Nevertheless, direct quantitative comparison between unimolecular and bimolecular processes is challenging because the entropy contributions to bimolecular reactions are often difficult to estimate accurately within standard DFT thermochemical treatments. Therefore, small differences in the calculated free energy barriers should be interpreted cautiously. Importantly, the experimental results clearly demonstrate that benzene C–H activation occurs under the conditions employed. Notably, C–H bond activation by nickel cluster systems possessing singlet ground states has also been discussed previously[68]. This provides additional context for the present findings.

For comparison, **1·benzene** was also used as the reference state in calculations of the C–H activation of benzene without dissociation of P^{t}Bu$_3$ (Supplementary Information Fig. S53), although this speculative pathway is inconsistent with experimental observations, which indicate that ligand exchange from P^{t}Bu$_3$ to benzene occurs prior to C–H activation. The resultant free energy barrier is 26.4 kcal mol^{-1}, which is somewhat higher than that proceeding through the pre-equilibrium intermediate ^{1}**I2** (20.0 kcal mol^{-1}) or an overall barrier from **1·benzene** (26.0 kcal mol^{-1}). From ^{1}**I2**, one could also envision an alternative pathway for intramolecular C–H activation of P^{t}Bu$_3$ (Supplementary Information Fig. S54). However, this route exhibits a higher barrier of 29.0 kcal mol^{-1} (^{1}**I2** → ^{1}**TS5**), rendering it an unlikely contributor to the observed reactivity.

Discussion

In this study, we synthesized and fully characterized a tetranuclear Ni(I)-hydride cluster, [Ni$_4$H$_4$(P^{t}Bu$_3$)$_4$] (**1**), which exhibits reversible intra- and inter-molecular C–H(D) bond activation. While previous studies, including seminal work by Johnson and co-workers on **[Ni$_5$]**, have demonstrated the potential of nickel-hydride species for C–H bond activation, cluster **1** expands this reactivity to unactivated aliphatic C–H bonds, such as those in *n*-octane, under mild conditions (50 °C). Unlike mono-nuclear Ni(I) complexes, which typically require challenging oxidative addition to access Ni(III) species, cluster **1** takes advantage of cooperative redox behavior of four Ni(I) centers to facilitate C–H(D) bond activation, leading to a formal Ni(I)$_2$Ni(II)$_2$ oxidation state. These findings overturn the conventional view of the limited capability of nickel in hydrocarbon activation, and provide a

conceptual foundation for the functionalization of C-H bonds under mild conditions.

Reversible H/D exchange was observed not only at hydrides but also within the supporting ligands, as revealed by mass spectrometry, providing mechanistic insights beyond those accessible via NMR alone. Moreover, ligand exchange experiments and DFT calculations indicate that replacement of one of the P^tBu_3 ligands with benzene occurs prior to the C–H(D) activation of benzene. The lability of P^tBu_3, together with the synthetic modularity of our system, distinguishes it from previously reported nickel cluster chemistry and opens new directions for the design of nickel clusters. Thus, our findings complement and extend prior works in the field, offering a versatile platform for exploring the reactivity and mechanistic diversity of nickel clusters in C–H activation chemistry.

Methods

General procedures

Unless otherwise noted, all reactions were performed in an inert Ar atmosphere using Schlenk techniques and a glove box (typical O_2 level, <1 ppm). Hexane, toluene, acetonitrile and tetrahydrofuran (THF) were purified over columns of activated alumina and supported copper catalyst purchased from Hansen & Co., Ltd. C_6D_6 and toluene-d_8 for NMR measurements was dried over sodium metal and distilled under reduced pressure before use. $[N^nBu_4][PF_6]$ was recrystallized from THF prior to use. Ni_3P powder (NII22PB, >99%(2N), fine powder) was purchased from Kojundo Chemical Laboratory Co. Ltd. for use as the Ni(I) reference sample for XAFS analysis. Nickel(II) tris-amide complex ($[Li(THF)_x][Ni\{N(SiMe_3)_2\}_3]$, $x \sim 4.5-5$)[47] and DBpin[56] were prepared according to the literature procedure. All other chemicals were purchased from commercial sources and used without further purification. ^1H, ^2H, ^{13}C, ^{31}P, and ^{11}B NMR spectra were recorded on Bruker AV400M or AV800 spectrometers, where observed signals were referenced to the residual peaks of the deuterated solvents, TMS (tetramethylsilane), or $BF_3{\cdot}Et_2O$, respectively. Fourier transform-infrared spectroscopy (FT-IR) was conducted using a Bruker Optics ALPHA FT-IR equipped with Diamond ATR. Electrospray ionization mass spectrometry (ESI-MS) was carried out using a Bruker SolariX FT-ICR-MS or compact spectrometers. UV-vis spectra were measured by a JASCO V-770 spectrophotometer. The deuterated products were analyzed by GC-MS using a Shimadzu 2010 Plus coupled with a QP2010 SE. Elemental analyses were performed using a J-SCIENCE MICRO CORDER JM11 for C, H and N determinations.

Synthesis of $[Ni_4H_4(P^tBu_3)_4]$ (1)

$[Li(THF)_x][Ni\{N(SiMe_3)_2\}_3]$ (12.0 g, 11.6 mmol; $x \sim 4.5-5$) was dissolved in toluene (10 mL) in a 100-mL round-bottom flask and stirred for 1 h at room temperature. To the solution, P^tBu_3 (4.70 g, 23.2 mmol, 2 equiv. to Ni) dissolved in 4 mL of toluene was added. The vial of the P^tBu_3 solution was rinsed with 1.0 mL of toluene, which was also added to the reaction mixture. The solution was stirred for 3 h, and the color of the solution gradually changed from dark red to dark green. To the solution, HBpin (5.5 mL, 38.3 mmol, 3.3 equiv. to Ni) was added over 20 mins while stirring at room temperature. During the addition, bubbling was observed due to the formation of gaseous H_2. Then, the solution was stirred for 24 h and filtered through a Whatman syringe filter (pore size: 0.45 µm). The supernatant was stored in the freezer at −35 °C for three days, yielding dark brown block crystals of **1·P^{t}Bu$_3$** (816 mg, 19%), which contains additional P^tBu_3 for crystal packing. Further purification was attained by rinsing with 1 mL of cold pentane, followed by extraction and recrystallization from pentane (15 mL) at −35 °C for 24 h, yielding dark brown needle-like block crystals of phosphine-free **1** (276 mg, 9%). ^1H NMR (in C_6D_6, 400 MHz, ppm): δ 2.60 ($P(CMe_3)_3$). $^{13}C\{^1H\}$ NMR (in C_6H_6 with a C_6D_6 capillary, 100 MHz, ppm): δ 65.74 ($P(CMe_3)_3$), 113.90 ($P(CMe_3)_3$). Note that no signal was observed in the ^{31}P NMR, likely due to significant broadening induced by direct interactions with magnetic centers (nickel atoms). UV-Vis (in toluene, λ_{max}, nm (ε, $cm^{-1}\,M^{-1}$)): 391 (1.9×10^4), 531 (5.9×10^3), 664, (3.5×10^3). Anal. Calcd. for $C_{48}H_{112}Ni_4P_4$: C, 55.01; H, 10.77; N, 0.00. Found: C, 54.96; H, 10.83; N, 0.00. FT-IR (ATR, cm^{-1}): ν 2992, 2966, 2950, 2889, 2863, 1479, 1469, 1442, 1396, 1387, 1356, 1172, 1019, 925, 807, 589, 562, 492, 424.

X-ray crystallographic analysis

Crystallographic data and refinement parameters of **1·P^{t}Bu$_3$** and **1** are listed in Table S3. Single crystals were covered with oil (Immersion Oil, type-B: code 1248, Cargile Laboratories, Inc.) and mounted on a MiTeGen MicroLoop. Diffraction data were collected under a cold N_2 stream (−150 °C), on a Rigaku RA-Micro 7 equipped with a PILATUS 200 K detector, using graphite-monochromated Mo Kα radiation (λ = 0.71075 Å). Eighteen preliminary images were taken at 0.5° increments of ω to evaluate the crystal quality and to determine pre-refined unit cell parameters, followed by full data collection also with 0.5° increments of ω. The raw frame data was processed using CrystalClear program, and the data sets were corrected for absorption using the REQAB program. The structure was solved with Intrinsic Phasing using SHELXT and refined by full-matrix least-square on F^2 using SHELXL in Olex2. All the non-hydrogen atoms were refined anisotropically. All the H atoms were refined isotropically. For the structural analysis of **1**, the twin law (−1 0 0; 0 −1 0; 0 0 −1) was applied with a 48.8(1.2)% contribution from a second domain. SIMU, RIGU, DELU, SADI, and FLAT were also applied to the disordered structural units. AFIX, DFIX, and SADI were applied to model hydrides due to significant structural disorder. The solvent molecules in **1** were SQUEEZED from the lattice using the Olex2 solvent mask command due to unresolvable disorder. A solvent mask was calculated, and 142 electrons were found in a volume of 714 Å^3 in the void per unit cell. This is consistent with the presence of one pentane, **1·[C$_5$H$_{12}$]**, per Asymmetric Unit which accounts for 168 electrons per unit cell. The cif file can be found at the Cambridge Crystallographic Data Centre (CCDC; https://www.ccdc.cam.ac.uk) under accession numbers CCDC 2422079 (**1·P^{t}Bu$_3$**) and 2422080 (**1**).

Ni *K*-edge X-ray absorption fine structure (XAFS)

The Ni *K*-edge XAFS measurements were conducted at beamlines BL01B1 of the SPring-8 facility of the Japan Synchrotron Radiation Research Institute (JASRI). The incident X-ray beam was monochromatized by a Si(111) double-crystal monochromator. As a reference, Ni foil, Ni_3P, and $Ni(II)Cl_2{\cdot}6H_2O$ were measured in transmission mode. XAFS spectra of **1** were measured in transmission mode at room temperature and 123 K using an ionization chamber as a detector. Low temperatures were controlled and maintained using a UNISOKU CoolSpeK in conjunction with a temperature controller and a gas flow controller. Obtained EXAFS spectra were analyzed by the xTunes program[69]. The k^3-weighted EXAFS spectra in the k range 3.0–16.0 Å for the Ni *K*-edge were Fourier transformed into r space for structural analysis. In the curve fitting analysis, the phase shifts and back-scattering amplitude functions of Ni–Ni, Ni–Cl, and Ni–P were calculated using the FEFF8.5 L program. The results of the curve fitting analysis are summarized in Table S5.

Electrochemical measurements

Cyclic voltammograms were recorded on a BAS ALS-660A electrochemical analyzer. All potentials were measured with reference to Ag/AgCl (Innovative Instruments, Inc.), and ferrocene (Fc) was used as an external standard. Each measurement was performed under the following conditions: sample concentration, 1 mM; solvent, THF; working electrode, glassy carbon; counter electrode, Pt; reference electrode, Ag/AgCl (Innovative Instruments, Inc.); supporting electrolyte, $[^nBu_4N][PF_6]$ (0.2 M); starting potential, rest potentials.

Magnetic measurements

The microcrystalline sample of **1** (49.5 mg) was sealed in a quartz tube with quartz wool, and the tube was flame-sealed before measurement. Susceptibility data were collected using a Quantum Design MPMS-5XL SQUID magnetometer. Magnetic data were corrected for the diamagnetism of the sample using Pascal's constants[70]. The diamagnetism of the sample holder and quartz wool was corrected using a blank sample tube without a compound. DC magnetization data for **1** were collected under applied dc magnetic fields at 1 T.

The solution magnetic susceptibility of **1** was determined by the Evans method, where 12 vol% cyclohexane in C_6D_6 was used as the solvent. Using this solvent, the ^{1}H NMR spectrum of **1** (2.3 mM) was measured at 298 K, in the presence of a sealed capillary containing the same solvent. The cyclohexane signals from the solution of **1** and from the capillary were observed, and their difference in the magnetic field was used to calculate the magnetic moment[50,51].

Electron spin resonance (ESR) measurements

For ESR measurements, a powder of **1** was loaded into quartz tubes (o.d. 3.0 mm) in an Ar-filled glovebox and sealed with a J-Young valve. Continuous wave (CW) X-band (9.4 GHz) spectra were collected using a Bruker E580 spectrometer equipped with a super high Q resonator (ER 4122SHQ). Cryogenic temperatures were controlled and maintained using an ESR900 liquid helium cryostat in conjunction with a temperature controller and a gas flow controller.

H/D exchange between 1 and deuterated solvents

General procedure. **1** (2.0 mg) was dissolved in 600 mg of a deuterated solvent (benzene-d_6, *n*-octane-d_{18}, cyclohexane-d_{12}, or toluene-d_8). The solution was transferred to a glass vessel, sealed, and heated at 50 °C for 24 h. After cooling to room temperature, an aliquot was diluted with THF and analyzed by ESI-MS (positive mode) to monitor the reaction progress.

Investigation of concentration effects. Samples were prepared by dissolving **1** (1.0, 2.0, 3.0, or 4.0 mg) in 600 mg of C_6D_6. Each solution was transferred to a glass vessel, sealed, and heated at 50 °C for 6, 12, 24, 36, or 48 h. After cooling, aliquots were diluted with THF and analyzed by ESI-MS.

Investigation of temperature effects. Samples were prepared by dissolving **1** (2.0 mg) in 600 mg of C_6D_6. Each solution was then transferred to a glass vessel and sealed. After heating the sample at 40, 50, 60, and 70 °C for 24 h, an aliquot was taken and diluted with THF, and the reaction progress was monitored by ESI-MS.

Hot filtration test. A mixture of **1** (5.0 mg, 5.0 µmol) and C_6D_6 (1500 mg) was prepared and divided equally into two glass vessels, which were sealed. Both samples were heated at 50 °C for 12 h, and the reaction progress was monitored by ESI-MS. One sample was then filtered through a Whatman syringe filter (0.45 µm pore size). Portions (600 µL) of both the filtered and unfiltered solutions were transferred to new glass vessels, sealed, and heated at 50 °C for an additional 12 h. After cooling, aliquots were diluted with THF and analyzed by ESI-MS.

H/D exchange between 1 and C_6D_6 in the presence of P^{t}Bu$_3$. **1** (2.0 mg) was dissolved in 600 mg of C_6D_6. P^{t}Bu$_3$ (1 or 10 equiv relative to **1**) was added, and the solution was transferred to a glass vessel, sealed, and heated at 50 °C for 24 h. After cooling, an aliquot was diluted with THF and analyzed by ESI-MS.

H/D exchange between C_6D_6 and toluene catalyzed by 1

Method A, at 50 °C. An NMR tube was charged with **1** (2.0 mg, 2.0 µmol), toluene (100 mg, 1 mmol, 500 eq.), and C_6D_6 (500 mg). A capillary containing a C_6D_6 solution of $SiMe_4$ was inserted into the tube as an external standard. The ^{1}H and ^{2}H NMR spectra were measured before starting the reaction. After heating the NMR tube at 50 °C for 24 h, the ^{1}H and ^{2}H NMR spectra were recorded. The intensity of the methyl group of toluene in the ^{1}H NMR decreased by 19.2% after heating (Fig. S41 top). Therefore, at least 96 times (500 eq. x 19.2%) of H/D exchange occurred for the methyl group of toluene. The volatile material was separated from the mixture by distillation and subjected to GC-MS analysis.

Method B, at 60 °C. An NMR tube was charged with **1** (2.0 mg, 2.0 µmol), toluene (100 mg, 1.0 mmol, 500 equiv), C_6D_6 (500 mg), and cyclododecane (16.8 mg, 100 µmol) as an internal standard. ^{1}H and ^{2}H NMR spectra were recorded prior to heating. The tube was then sealed and heated at 60 °C for 24 h. After cooling to room temperature, a capillary containing a C_6D_6 solution of $SiMe_4$ was inserted for helping d-locking of the measurement and as a chemical shift reference. Then, the ^{1}H and ^{2}H NMR spectra were recorded. The intensity of the methyl signal of toluene in the ^{1}H NMR spectrum decreased by 42.3% after heating. On this basis, the extent of H/D exchange at the methyl position of toluene was estimated to be at least 211 turnovers (500 eq. ×42.3%).

Computational methods. Ground state geometry optimizations were performed for the $S = 0$, 1, and 2 states of the Ni cluster (**1**) using density functional theory (DFT), as implemented in the ORCA (Version 6.0)[71]. The ZORA scalar relativistic method was employed[72]. The BP86-D3BJ functional[52,53], including the Grimme's dispersion and Becke-Johnson damping[73,74], ZORA-def2-TZVP basis sets and SARC/J auxiliary basis sets were used for all atoms[75–77]. An implicit solvent model, specifically a conductor-like continuum polarization model (C-PCM) was used[78], where toluene was used as the solvent. Starting from the BP86-D3BJ optimized ground-state structures, vertical excitation energies were computed using the time-dependent density functional theory (TDDFT), based on the BP86-D3BJ optimized geometries. The B3LYP functional[79,80], employing the Grimme's dispersion and Becke-Johnson damping, ZORA-def2-TZVP basis sets and SARC/J auxiliary basis, C-PCM were used for TDDFT calculations.

To investigate the mechanism for the C−H bond activation of benzene and P^{t}Bu$_3$ unit, two-layer *O*ur own *N*-layered *I*ntegrated molecular *O*rbital and *M*olecular mechanics (ONIOM) method[81,82], as implemented in the ORCA program, was used. Partitioning of the molecular systems is shown in Fig. S48. For the ONIOM-high layer, BP86-D3BJ functional, the ZORA-def2-TZVP basis sets, and SARC/J auxiliary basis sets were employed. The Geometries, Frequencies, and Non-covalent Interactions Tight Binding (GNF1-xTB) method[83] was applied for the ONIOM-low layer. All reported free energies include thermal corrections evaluated at 298.15 K and 1 atm. Potential energy of the optimized structures was calculated as the single-point energy, employing the BP86-D3BJ functional, ZORA-def2-TZVP basis sets, SARC/J auxiliary basis, and C-PCM for all atoms.

The Kinetic Isotope Effect (KIE) was computed using the following formula:

$$\frac{k_H}{k_D} = e^{-\left(\Delta G^{\ddagger}_H - \Delta G^{\ddagger}_D\right)/RT}$$

where:

k_H = rate constant for the reaction involving hydrogen

k_D = rate constant for the reaction involving deuterium

$\Delta G_H^{\ddagger}$ = Gibbs free energy of activation for the reaction involving hydrogen

$\Delta G_D^{\ddagger}$ = Gibbs free energy of activation for the reaction involving deuterium

R = universal gas constant

T = temperature in Kelvin

Data availability

The X-ray crystallographic coordinates for the structures reported in this study have been deposited at the Cambridge Crystallographic Data Centre (CCDC) under deposition numbers 2422079 (**1·P^{t}Bu$_3$**) and 2422080 (**1**). These data can be obtained free of charge from the Cambridge Crystallographic Data Centre via www.ccdc.cam.ac.uk/data_request/cif. The data supporting the findings of this study are provided in the Article and Supplementary Information. Source data are provided with this paper. All data are available from the corresponding author upon request. Source data are provided with this paper.

References

1. Norton, J. R. & Sowa, J. Introduction: metal hydrides. *Chem. Rev.* **116**, 8315–8317 (2016).
2. Moore, D. S. & Robinson, S. D. Hydrido complexes of the transition metals. *Chem. Soc. Rev.* **12**, 415–452 (1983).
3. Suzuki, H. Activation of organic substrates on multi-metallic sites of transition metal polyhydride clusters having C_5Me_5 groups as auxiliary ligands. *Eur. J. Inorg. Chem.* **2002**, 1009–1023 (2002).
4. Adams, R. D. & Captain, B. Hydrogen activation by unsaturated mixed-metal cluster complexes: new directions. *Angew. Chem. Int. Ed.* **47**, 252–257 (2008).
5. Ohki, Y. et al. $Co_6H_8(P^iPr_3)_6$: a cobalt octahedron with face-capping hydrides. *Angew. Chem. Int. Ed.* **55**, 15821–15825 (2016).
6. Plois, M. et al. Open-shell first-row transition-metal polyhydride complexes based on the fac-$[RuH_3(PR_3)_3]^-$ building block. *Angew. Chem. Int. Ed.* **52**, 1314–1318 (2013).
7. Hu, S., Shima, T. & Hou, Z. Carbon-carbon bond cleavage and rearrangement of benzene by a trinuclear titanium hydride. *Nature* **512**, 413–415 (2014).
8. Campos, J. et al. A carbene-rich but carbonyl-poor $[Ir_6(Ime)_8(CO)_2H_{14}]^{2+}$ polyhydride cluster as a deactivation product from catalytic glycerol dehydrogenation. *Angew. Chem. Int. Ed.* **53**, 12808–12811 (2014).
9. Gieshoff, T. N. et al. Alkene hydrogenations by soluble iron nanocluster catalysts. *Angew. Chem. Int. Ed.* **56**, 3585–3589 (2017).
10. Shima, T. et al. Dinitrogen Activation and Hydrogenation by $C_5Me_4SiMe_3$-Ligated Di- and Trinuclear Chromium Hydride Complexes. *J. Am. Chem. Soc.* **142**, 9007–9016 (2020).
11. Hu, S., Shima, T. & Hou, Z. Hydrodeoxygenative cyclotetramerization of carbon monoxide by a trinuclear titanium polyhydride complex. *J. Am. Chem. Soc.* **142**, 19889–19894 (2020).
12. Muhr, M. et al. Catalytic alkyne semihydrogenation with polyhydride Ni/Ga Clusters. *Angew. Chem. Int. Ed.* **62**, e202308790 (2023).
13. Brayshaw, S. K. et al. $[Rh_7(PiPr_3)_6H_{18}][BArF_4]_2$: a molecular Rh(III) surface decorated with 18 hydrogen atoms. *Angew. Chem. Int. Ed.* **46**, 7844–7848 (2007).
14. Takano, S. et al. Hydride doping of chemically modified gold-based superatoms. *Acc. Chem. Res.* **51**, 3074–3083 (2018).
15. Zavras, A. et al. Synthesis, structure, and gas-phase reactivity of a silver hydride complex $[Ag_3\{(PPh_2)_2CH_2\}_3(\mu_3\text{-}H)(\mu_3\text{-}Cl)]BF_4$. *Angew. Chem. Int. Ed.* **52**, 8391–8394 (2013).
16. Wang, S. et al. Deep learning accelerated determination of hydride locations in metal nanoclusters. *Angew. Chem. Int. Ed.* **60**, 12289–12292 (2021).
17. Shima, T. et al. Dinitrogen cleavage and hydrogenation by a trinuclear titanium polyhydride complex. *Science* **340**, 1549–1552 (2013).
18. Shima, T., Zhuo, Q. & Hou, Z. Dinitrogen activation and transformation by multimetallic polyhydride complexes. *Coord. Chem. Rev.* **472**, 214766 (2022).
19. Shima, T. et al. Hydroamination of alkenes with dinitrogen and titanium polyhydrides. *Nature* **632**, 307–312 (2024).
20. Araake, R. et al. $[Fe_4]$ and $[Fe_6]$ hydride clusters supported by phosphines: synthesis, characterization, and application in N_2 reduction. *J. Am. Chem. Soc.* **139**, 5596–5606 (2017).
21. Eberhardt, N. A. & Guan, H. Nickel hydride complexes. *Chem. Rev.* **116**, 8373–8426 (2016).
22. Johnson, S. A. Nickel complexes for catalytic C–H bond functionalization. *Dalton Trans* **44**, 10905–10913 (2015).
23. Shoshani, M. M. & Johnson, S. A. Cooperative carbon-atom abstraction from alkenes in the core of a pentanuclear nickel cluster. *Nat. Chem.* **9**, 1282–1285 (2017).
24. Beck, R. et al. Catalytic hydrogen/deuterium exchange of unactivated carbon-hydrogen bonds by a pentanuclear electron-deficient nickel hydride cluster. *Angew. Chem. Int. Ed.* **51**, 11753–11756 (2012).
25. Shoshani, M. M., Liu, J. & Johnson, S. A. Mechanistic Insight into H/D Exchange by a Pentanuclear Ni–H Cluster and Synthesis and Characterization of Structural Analogues of Potential Intermediates. *Organometallics* **37**, 116–126 (2018).
26. Simoes, J. A. M. & Beauchamp, J. L. Transition metal-hydrogen and metal-carbon bond strengths: the keys to catalysis. *Chem. Rev.* **90**, 629–688 (1990).
27. Ogo, S. et al. A dinuclear Ni(μ-H)Ru complex derived from H_2. *Science* **316**, 585–587 (2007).
28. Manz, D.-H. et al. Pairwise H_2/D_2 exchange and H_2 substitution at a bimetallic dinickel(II) complex featuring two terminal hydrides. *J. Am. Chem. Soc.* **139**, 16720–16731 (2017).
29. Velian, A. et al. Synthesis and C-C coupling reactivity of a dinuclear Ni^I-Ni^I complex supported by a terphenyl diphosphine. *J. Am. Chem. Soc.* **132**, 6296–6297 (2010).
30. Zhou, Y.-Y. & Uyeda, C. Catalytic reductive [4+1]-cycloadditions of vinylidenes and dienes. *Science* **363**, 857–862 (2019).
31. Eaton, M. C. et al. Evaluating metal ion identity on catalytic silylation of dinitrogen using a series of trimetallic complexes. *Eur. J. Inorg. Chem.* **2020**, 1519–1524 (2020).
32. Matsuoka, Y. et al. Silylation of N_2 catalyzed by cubic $[Mo_3S_4Ni]$ clusters bearing Mo-bound cyclopentadienyl ligands. *Coordination Chemistry Research* **1**, 100001 (2025).
33. Takada, K., Maeda, H., Fukui, N. & Nishihara, H. Electrically conductive multivariate coordination nanosheets. *Coordination Chemistry Research* **1**, 100006 (2025).
34. Shoshani, M. M. et al. Synthesis of surface-analogue square-planar tetranuclear nickel hydride clusters and bonding to μ_4-NR, -O and -BH ligands. *Inorg. Chem.* **57**, 2438–2446 (2018).
35. Müller, J. et al. Tetrakis(η-cyclopentadienyl)tetranickel trihydride—An unusual tetranuclear cluster. *Angew. Chem. Int. Ed.* **12**, 1005–1006 (1973).
36. Huttner, G. & Lorenz, H. Die Struktur des Nickel-Clusters $H_3(C_5H_5)_4Ni_4$. *Chem. Ber.* **107**, 996–1008 (1974).
37. Pasynkiewicz, S., Buchowicz, W., Pietrzykowski, A. & Głowiak, T. The activation of C-H bonds in terminal olefins by cyclopentadienylnickel species. *J. Organomet. Chem.* **536–537**, 249–256 (1997).
38. Schneider, J. J., Goddard, R., Krüger, C., Werner, S. & Metz, B. Metallatome in der Synthese von Metallclustern, II1) Reaktionen von substituierten Cyclopentadienen und Nickelocen mit Nickel- und Eisenatomen. *Chem. Ber.* **124**, 301–308 (2006).
39. Ceriotti, A., Chini, P., Della Pergola, R. & Longoni, G. Carbonyl nickelates. 3. Synthesis and chemical characterization of the $[Ni_{12}(CO)_{21}H_{4-n}]n^-$ (n=2, 3, 4) clusters. *Inorg. Chem.* **22**, 1595–1598 (2002).
40. Chini, P. Large metal carbonyl clusters (LMCC). *J. Organomet. Chem.* **200**, 37–61 (1980).
41. Cesari, C., Shon, J. H., Zacchini, S. & Berben, L. A. Metal carbonyl clusters of groups 8–10: Synthesis and catalysis. *Chem. Soc. Rev.* **50**, 9503–9539 (2021).

42. Ohki, Y., Takikawa, Y., Hatanaka, T. & Tatsumi, K. Reductive N-N bond cleavage of diphenylhydrazine and azobenzene induced by coordinatively unsaturated Cp*Fe{N(SiMe$_3$)$_2$}. *Organometallics* **25**, 3111–3113 (2006).
43. Higaki, T. et al. An icosahedral 55-atom iron hydride cluster protected by tri-tert-butylphosphines. *J. Am. Chem. Soc.* **147**, 3215–3222 (2025).
44. Chakraborty, U. et al. Planar iron hydride nanoclusters: Combined spectroscopic and theoretical insights into structures and building principles. *ChemistryOpen* **10**, 265–271 (2021).
45. Faust, M. et al. The instability of Ni{N(SiMe$_3$)$_2$}$_2$: A fifty-year-old transition metal silylamide mystery. *Angew. Chem. Int. Ed.* **54**, 12914–12917 (2015).
46. Lipschutz, M. I. & Tilley, T. D. Synthesis and reactivity of a conveniently prepared two-coordinate bis(amido) nickel(II) complex. *Chem. Commun.* **48**, 7146–7148 (2012).
47. Reckziegel, A. et al. Intricate road to linear anionic nickel(I) hexamethyl-disilazanide [Ni(N(SiMe$_3$)$_2$)$_2$]$^-$. *Inorg. Chem.* **61**, 7794–7803 (2022).
48. Cordero, B. et al. Covalent radii revisited. *Dalton Trans.* 2832–2838 (2008).
49. Koetzle, T. F. et al. Neutron diffraction analysis of the structure of $H_3Ni_4(C_5H_5)_4$. *J. Am. Chem. Soc.* **101**, 5631–5637 (2002).
50. Evans, D. F. The determination of the paramagnetic susceptibility of substances in solution by nuclear magnetic resonance. *J. Chem. Soc.* 2003–2005 (1959).
51. Britovsek, G. J. P. et al. Cationic 2,6-bis(imino)pyridine iron and cobalt complexes. *J. Chem. Soc., Dalton Trans.* 1159–1171 (2002).
52. Perdew, J. P. Density-functional approximation for the correlation energy of the inhomogeneous electron gas. *Phys. Rev. B* **33**, 8822–8824 (1986).
53. Becke, A. D. Density-functional exchange-energy approximation with correct asymptotic behavior. *Phys. Rev. A* **38**, 3098–3100 (1988).
54. Fujita, S. et al. Ni_2P nanoalloy as an air-stable and versatile hydrogenation catalyst in water. *Chem. Eur. J.* **27**, 4439–4446 (2021).
55. Al Rashid, M. H. et al. X-ray absorption fine structure studies on nickel phosphide catalysts. *Radiat. Phys. Chem.* **189**, 109727 (2021).
56. Wei, C. S. et al. Origins of the selectivity for borylation of primary over secondary C–H bonds. *J. Am. Chem. Soc.* **132**, 3078–3091 (2010).
57. Hartwig, J. F. Regioselectivity of the borylation of alkanes and arenes. *Chem. Soc. Rev.* **40**, 1992–2002 (2011).
58. Hartwig, J. F. Borylation and silylation of C–H bonds. *Acc. Chem. Res.* **45**, 864–873 (2012).
59. Bisht, R. et al. Metal-catalysed C–H bond activation and borylation. *Chem. Soc. Rev.* **51**, 5042–5100 (2022).
60. Ros, A. et al. Functional group directed C–H borylation. *Chem. Soc. Rev.* **43**, 3229–3243 (2014).
61. Cook, A. K., Schimler, S. D., Matzger, A. J. & Sanford, M. S. Catalyst-controlled selectivity in the C–H borylation of methane and ethane. *Science* **351**, 1421–1424 (2016).
62. Smith, K. T. et al. D. J. Catalytic borylation of methane. *Science* **351**, 1424–1427 (2016).
63. Oeschger, R. et al. Diverse functionalization of strong alkyl C–H bonds by undirected borylation. *Science* **368**, 736–741 (2020).
64. Higashi, T., Kusumoto, S. & Nozaki, K. Heterolytic oxidative addition of sp^2 and sp^3 C–H bonds. *J. Am. Chem. Soc.* **143**, 12999–13004 (2021).
65. Harry, N. A. et al. Recent advances and prospects in nickel-catalyzed C–H activation. *Catal. Sci. Technol.* **9**, 1726–1743 (2019).
66. Chatani, N. Nickel-catalyzed functionalization reactions involving C–H bond activation. *Acc. Chem. Res.* **56**, 3053–3064 (2023).
67. Zarate, C. et al. Ni(I)−X Complexes Bearing a Bulky α-Diimine Ligand: Synthesis, Structure, and Superior Catalytic Performance in the Hydrogen Isotope Exchange in Pharmaceuticals. *J. Am. Chem. Soc.* **141**, 5034–5044 (2019).
68. Sharma, S., Pandey, B. & Rajaraman, G. The interplay of covalency, cooperativity, and coupling strength in governing C–H bond activation in Ni_2E_2 (E= O, S, Se, Te) complexes. *Chem. Sci.* **15**, 10529–10540 (2024).
69. Asakura, H. et al. xTunes: A new XAS processing tool for detailed and on-the-fly analysis. *Radiat. Phys. Chem.* **175**, 108270 (2020).
70. Bain, G. A. & Berry, J. F. Diamagnetic Corrections and Pascal's Constants. *J. Chem. Educ.* **85**, 532–536 (2008).
71. Neese, F. Software update: The ORCA program system—Version 5.0. *WIREs Computational Molecular Science* **12**, e1606 (2022).
72. Neese, F., Wennmohs, F., Becker, U. & Riplinger, C. The ORCA quantum chemistry program package. *J. Chem. Phys.* **152**, 224108 (2020).
73. Grimme, S., Antony, J., Ehrlich, S., Krieg, H. A consistent and accurate ab initio parametrization of density functional dispersion correction (DFT-D) for the 94 elements H-Pu. *J. Chem. Phys.* **132**, 154104.
74. Pantazis, D. A. & Neese, F. All-electron scalar relativistic basis sets for the actinides. *J. Chem. Theory Comput.* **7**, 677–684 (2011).
75. Weigend, F. & Ahlrichs, R. Balanced basis sets of split valence, triple zeta valence and quadruple zeta valence quality for H to Rn: Design and assessment of accuracy. *Phys. Chem. Chem. Phys.* **7**, 3297–3305 (2005).
76. Weigend, F. Accurate coulomb-fitting basis sets for H to Rn. *Phys. Chem. Chem. Phys.* **8**, 1057–1065 (2006).
77. Pantazis, D. A., Chen, X. Y., Landis, C. R. & Neese, F. All-electron scalar relativistic basis sets for third-row transition metal atoms. *J. Chem. Theory Comput.* **4**, 908–919 (2008).
78. Barone, V. & Cossi, M. Quantum calculation of molecular energies and energy gradients in solution by a conductor solvent model. *J. Phys. Chem. A* **102**, 1995–2001 (1998).
79. Lee, C., Yang, W. & Parr, R. G. Development of the Colle-Salvetti correlation-energy formula into a functional of the electron density. *Phys Rev B* **37**, 785–789 (1988).
80. Miehlich, B., Savin, A., Stoll, H. & Preuss, H. Results obtained with the correlation energy density functionals of becke and Lee, Yang and Parr. *Chem. Phys. Lett.* **157**, 200–206 (1989).
81. Chung, L. W. et al. The ONIOM method and its applications. *Chem. Rev.* **115**, 5678–5796 (2015).
82. Sameera, W. M. C. & Maseras, F. Expanding the range of force fields available for ONIOM Calculations: The SICTWO Interface. *J. Chem. Inf. Model.* **58**, 1828–1835 (2018).
83. Grimme, S., Bannwarth, C. & Shushkov, P. A robust and accurate tight-binding quantum chemical method for structures, vibrational frequencies, and noncovalent interactions of large molecular systems parametrized for all spd-Block Elements (Z = 1-86). *J. Chem. Theory Comput.* **13**, 1989–2009 (2017).

Acknowledgements

We thank Ms. Ayaka Maeno, Ms. Yuki Nakajima, and Dr. Keisuke Tao-Kakuyama for the assistance in the NMR measurements, and Ms. Toshiko Hirano for the assistance in the elemental analysis.

Author contributions

K. S., T. H., K. T., R. Y., and H. I. conducted the experiments. W. M. C. S. collected and analyzed the computational data. R. T., T. T., S. K., and S. Y. collected and analyzed the X-ray absorption data. T. S. and M. N. collected and analyzed the solid-state magnetic data. T. K. collected and analyzed the ESR data. Y. O. designed the study. K. S., T. H., and Y. O. wrote the manuscript with input from all authors.

Funding

This work was financially supported by Grant-in-Aids for Scientific Research (23H01974 and 25K22274 for Y.O., 22K20558 and 23K13707 for T.H., 23K13763 and 25K18050 for H.I., 24H00053 for T.T., and 24H02217

for S.Y.) from the Japanese Ministry of Education, Culture, Sports, Science and Technology (MEXT), CREST grant (JPMJCR21B1 for Y.O. and JPMJCR21B4 for T.T.) from JST, the Yazaki Memorial Foundation and Toshiaki Ogasawara Memorial Foundation (for Y.O.), and the Tokuyama Science Foundation (for T.H.). This work was also supported by the International Collaborative Research Program of Institute for Chemical Research, Kyoto University (2024-7 for WMCS/YO and 2023-14 for TS/TH). This study was carried out with the NMR spectrometer in the JURC at Institute for Chemical Research, Kyoto University. The iJURC at ICR, Kyoto University provided support for the FT-ICR-MS measurements. The ESR measurements were conducted at Institute for Molecular Science, supported by "Advanced Research Infrastructure for Materials and Nanotechnology in Japan (ARIM)" of the Ministry of Education, Culture, Sports, Science and Technology (MEXT) (Proposal Number: JPMXP1223MS1085). The XAFS measurements were conducted at SPring-8 with the approval of JASRI (2023B2070 and 2024A1775).

Competing interests

The authors declare no competing interests.

Additional information

Supplementary information The online version contains supplementary material available at https://doi.org/10.1038/s41467-026-76006-4.

Correspondence and requests for materials should be addressed to Tatsuya Higaki, W. M. C. Sameera or Yasuhiro Ohki.

Peer review information *Nature Communications* thanks Manar Shoshani and the other, anonymous, reviewer(s) for their contribution to the peer review of this work. A peer review file is available.